Obrabotka metallov (tekhnologiya, oborudovanie, instrumenty) = Metal Working and Material Science. 2026 vol. 28 no. 3 pp. 345–359
ISSN: 1994-6309 (print) / 2541-819X (online)
DOI: 10.17212/1994-6309-2026-28.3-345-359

NSTU NETI

Obrabotka metallov - Metal Working and Material Science

Journal homepage: http://journals.nstu.ru/obrabotka_metallov

Structure and wear resistance of hot-rolled Fe–Cr–B coatings

Alina Dudareva [1, a, *], *Ekaterina Esikova* [1, b], *Sergey Stankevich* [1, c], *Vladislav Shikalov* [1, d], *Yulia Malyutina* [1, 2, e], *Maxim Khomyakov* [3, f], *Evgeny Domarov* [4, g], *Kemal Emurlaev* [1, 5, h]

[1] Novosibirsk State Technical University, 20 Prospekt K. Marksa, Novosibirsk, 630073, Russian Federation
[2] Lavrentyev Institute of Hydrodynamics of the Siberian Branch of the RAS, 15 Ac. Lavrentieva ave., Novosibirsk, 630090, Russian Federation
[3] Institute of Laser Physics of the Siberian Branch of the RAS, 13 Ac. Lavrentieva ave., Novosibirsk, 630090, Russian Federation
[4] Budker Institute of Nuclear Physics of Siberian Branch Russian Academy of Sciences, 11 Acad. Lavrentieva Pr., Novosibirsk, 630090, Russian Federation
[5] Siberian Circular Photon Source "SKIF" Boreskov Institute of Catalysis of Siberian Branch of the Russian Academy of Sciences (SRF "SKIF"), 1 Nikol'skii pr., Kol'tsovo, 630559, Russian Federation

[a] https://orcid.org/0009-0001-5649-7090, dudareva-alina@mail.ru; [b] https://orcid.org/0009-0004-2000-3695, kate.esikova@mail.ru;
[c] https://orcid.org/0009-0004-0964-319X, stankevich.2016@corp.nstu.ru; [d] https://orcid.org/0000-0002-0491-2803, v.shikalov@gmail.com;
[e] https://orcid.org/0000-0002-0305-7518, romashova@corp.nstu.ru; [f] https://orcid.org/0000-0001-8095-2092, mnkhomy@ya.ru;
[g] https://orcid.org/0000-0003-2422-1513, domarov88@mail.ru; [h] https://orcid.org/0000-0002-1114-6799, emurlaev@corp.nstu.ru

ARTICLE INFO

Article history:
Received: 05 June 2026
Revised: 23 June 2026
Accepted: 14 August 2026
Available online: 15 September 2026

Keywords:
Chromium-nickel austenitic steel
Electron beam cladding
Hot plastic deformation
Chromium
Boron

Funding
This study was supported by the Russian Science Foundation grant No. 23-79-00066, https://rscf.ru/project/23-79-00066/.
The synchrotron X-ray experiments were carried out at the shared research center *SSTRC* based at the *VEPP-4 – VEPP-2000* complex at *BINP SB RAS*. This work was partially supported by the Ministry of Science and Higher Education of the Russian Federation within the governmental assignment for *SRF SKIF Boreskov Institute of Catalysis* (project FWUR-2026-0002).

Acknowledgements
The structural research was carried out at the core facility "Structure, mechanical and physical properties of materials", *NSTU*.
Synchrotron X-ray research was conducted at the shared research center *SSTRC* on the basis of the *VEPP-4–VEPP-2000* complex at *BINP SB RAS*.

ABSTRACT

Introduction. Austenitic steels are widely used in mining, railway, and chemical industries due to their high toughness and corrosion resistance. However, their service life under severe wear conditions is limited, which necessitates the development of effective surface hardening techniques that preserve the ductility of the substrate. ***The purpose of this study*** is to investigate the microstructure, mechanical properties, and tribological behavior of *Fe–Cr–B*-based coatings fabricated by non-vacuum electron beam cladding on *AISI 321* steel followed by combined treatment (quenching and hot rolling). **Materials and methods.** Cladding was performed using two powder mixtures with different boron contents: *C1QHR* (1 g *B*) and *C2QHR* (2 g *B*). After cladding, the samples were quenched from 1,100 °C and subsequently hot-rolled at 950 °C. The microstructure was examined using scanning electron microscopy, and the phase composition was determined by X-ray diffraction. Mechanical properties were evaluated by microhardness measurements, while tribological characteristics were assessed using a ball-on-flat dry sliding wear test. **Results and discussion.** The combined treatment was found to promote the precipitation of submicron $(Fe,Cr)_{23}C_6$ carbides within the austenitic matrix and the formation of $(Fe,Cr)_2(C,B)$ carboborides. The coating with the higher boron content (*C2QHR*) exhibited a hardness of 484 ± 20 HV, which is 2.4 times higher than that of *AISI 321* steel. The wear resistance of the *C2QHR* coating is 5.3 times higher than that of the *AISI 321* steel substrate. The main mechanisms enhancing the wear resistance of the coatings are precipitation hardening due to carbide precipitation, as well as the formation of borides and carboborides. ***Conclusions.*** The combination of quenching and hot rolling of the layers obtained by non-vacuum electron beam cladding forms a wear-resistant protective layer on the surface of *AISI 321* steel.

For citation: Dudareva A.A., Esikova E.D., Stankevich S.V., Shikalov V.S., Malyutina Yu.N., Khomyakov M.N., Domarov E.V., Emurlaev K.I. Structure and wear resistance of hot-rolled Fe–Cr–B coatings. *Obrabotka metallov (tekhnologiya, oborudovanie, instrumenty) = Metal Working and Material Science*, 2026, vol. 28, no. 3, pp. 345–359. DOI: 10.17212/1994-6309-2026-28.3-345-359. (In Russian).

*** Corresponding author**
Dudareva Alina A., Post-graduate Student
Novosibirsk State Technical University,
20 Prospekt K. Marksa,
630073, Novosibirsk, Russian Federation
Tel.: +7 913 707-63-44, **e-mail:** dudareva-alina@mail.ru

Introduction

Austenitic steels are widely used in critical industries such as mining, railway, automotive, and aerospace. Their advantages include high fracture toughness, corrosion resistance, and manufacturability. However, low hardness and the resultant insufficient abrasive wear resistance significantly restrict the durability of components [1–3]. Although a wide range of wear-resistant materials currently exists [2, 4–7], many of them are either insufficiently effective under severe wear conditions or involve considerable cost.

One possible solution to the problem of improving the wear resistance of steel surfaces is the formation of coatings based on the *Fe–Cr–C–B* system. Such alloys are characterized by high hardness and abrasive wear resistance [8–10]. In high-chromium alloys, the primary crystallizing phases are hard compounds such as Me_7C_3, Me_3B, and Me_3B_2 [11], which exhibit hardness values in the range of 1,300–2,000 HV [9, 12]. Despite their high hardness and strength, borides are prone to cracking during heat treatment. Alloying *Fe–Cr–C–B* system alloys with chromium prevents the embrittlement of borides [13]. Studies of the *Fe–0.8B–1.3C–1.6Cr* (wt.%) alloy have shown that thermomechanical treatment enables the refinement of the coarse cast microstructure into a fine-grained ferritic matrix with fine borocarbide particles of the $Me_{23}(C,B)_3$ type [14]. Increasing the quenching temperature of the cast *Fe–Cr–B* alloy from 900 to 950 °C ensures the transition from a pearlite-martensite structure to a fully martensitic one. For the cast *Fe–Cr–B* alloy, it has been established that quenching at 1,000 °C causes spheroidization of the $(Cr,Fe)_2(C,B)_3$ borocarbide, partial decomposition of the Fe_2B phase, and uniform distribution of the eutectic phase in the structure [15]. Heating to 1,100 °C followed by rapid cooling leads to transformation of the metallic matrix into a fine-needle martensite structure, while the excess $(Cr,Fe)_2(C,B)_3$ and Fe_2B phases remain in the structure, contributing additional hardening [16].

The resulting structure directly determines the tribological properties of *Fe–Cr–B* alloys. It was shown in [17] that boron alloying significantly improves wear resistance, with the wear rate decreasing tenfold relative to the boron-free specimen. Nevertheless, the dependence of wear on boron concentration was found to be non-monotonic. This is corroborated by study [18], which confirmed that boron addition increases wear resistance under dry sliding due to high hardness and the formation of boride phases. At the same time, the specific wear rates of the alloys decrease with increasing boron content and then increase again due to the embrittlement caused by excessive alloying.

Thus, the *Fe–Cr–B* system is of considerable interest for the development of wear-resistant coatings. Quenching is necessary to dissolve the coarse phases formed during solidification. Subsequent hot rolling refines the microstructure and eliminates casting inhomogeneity. Combined treatment enables the formation of a structure with an optimal balance of hardness and ductility. Despite a significant number of studies on *Fe–Cr–B* alloys, the effect of boron concentration on structure formation and the tribological properties of coatings fabricated by non-vacuum electron beam cladding followed by hot rolling has not been investigated. In particular, there is a lack of data on the influence of boron content on the phase constitution, morphology of the hardening phases, and wear resistance of hot-rolled coatings.

The purpose of this work is to establish the effect of boron content on the structure, mechanical and tribological properties of *Fe–Cr–B* coatings formed by non-vacuum electron beam cladding followed by combined treatment (quenching and hot rolling).

The specific tasks of this study were:

– to fabricate *Fe–Cr–B*-based coatings on *AISI 321* steel by non-vacuum electron beam cladding followed by combined treatment (quenching and hot rolling);

– to characterize the phase composition and microstructure of the obtained coatings after combined treatment;

– to evaluate the wear resistance of the fabricated coatings.

Experimental procedure

Surface alloying of flat workpieces was carried out using non-vacuum electron beam cladding (Fig. 1). This technology enables the formation of composite materials of the “substrate – cladded layer (coating)” type with a thickness of up to several millimeters in a single pass [19–21].

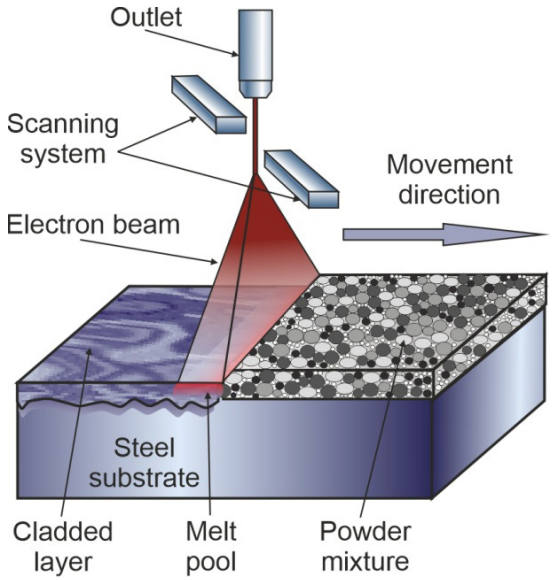

Fig. 1. Schematic diagram of the non-vacuum electron beam cladding process

In this work, plates of austenitic chromium-nickel *AISI 321* steel with dimensions of 50×100×12 mm were used as the substrate material. The coatings were fabricated from powder mixtures, the compositions of which are given in Table 1. Powder mixtures of *Cr–B* were cladded onto the steel substrates by means of non-vacuum electron beam cladding. The chromium content in the powder mixtures was kept constant, while the boron mass in coating *C2QHR* was twice that in *C1QHR*. This approach was expected to reduce the solidification temperature of the *Fe–Cr–B* system due to an increase in the fraction of the eutectic melt. A further motivation for increasing the boron content was related to the interaction of boron with chromium carbides, specifically to suppress their growth at grain boundaries [22–25]. To prevent oxidation of the melt pool, MgF_2 flux was added to the powder mixture. Cladding was carried out in air using a relativistic electron beam generated by an *ELV-6* industrial accelerator (*Budker Institute of Nuclear Physics SB RAS*, Novosibirsk), under the following parameters: scanning frequency – 50 Hz, distance from the emitter to the workpiece – 90 mm. The cladding parameters are given in Table 1.

Table 1

Compositions of powder mixtures and parameters of the electron beam cladding process

Samples designation	Composition of the powder mixture (g)			Cladding parameters			
	Cr	B	MgF_2	Electron energy (MeV)	Beam current (mA)	Power density (kJ/cm^2)	Specimen traverse speed (mm/s)
C1QHR	1,5	1	2,5	2	18	7,2	10
	30 %	20 %	50 %				
C2QHR	1,5	2	3,5				
	21 %	29 %	50 %				

To increase hardness and wear resistance, the obtained coatings were quenched and then hot rolled. Heating for quenching was performed in a *Nabertherm LH120/14* furnace in air. The samples were heated to 1,100 °C, held for 30 min, and water-quenched. The cladded coatings together with the substrate were subjected to hot plastic deformation at 950 °C on a "Quarto" rolling mill. Deformation was repeated until crack formation occurred in the coatings, which served as the failure criterion. The true strain was $\bar{\varepsilon}_\Sigma = 0.96$ for *C1QHR* and $\bar{\varepsilon}_\Sigma = 0.67$ for *C2QHR*. The final thickness of the cladded layer after deformation was 1.4 mm and 2.5 mm for *C1QHR* and *C2QHR*, respectively.

The microstructure of the coatings was studied using a *Carl Zeiss AxioObserver Z1m* optical microscope. The grain structure was revealed by etching in an HNO_3:*HCl* solution (1:3 by volume). Detailed structural characterization was carried out using a *Carl Zeiss EVO50 XVP* scanning electron microscope equipped with an *Oxford Instruments X-Act* attachment for energy-dispersive X-ray spectroscopy (*EDX*). The fraction of structural constituents was estimated by the point counting method (*ASTM E562*) using *JMicroVision 1.3.4* software.

To determine the phase composition, diffraction patterns were obtained using synchrotron X-ray radiation at the "High-pressure X-ray diffraction" beamline of the *VEPP-3 / VEPP-4* complex *(Budker Institute of Nuclear Physics SB RAS*, Novosibirsk). The photon energy was 30 keV. Diffraction patterns were recorded using a *Mar345* two-dimensional detector, featuring a resolution of 3,500×3,500 pixels and a pixel size of 75 μm. The exposure time was set to 10 min. The two-dimensional ring patterns were azimuthally integrated using the *pyFAI* module implemented in *Python*.

Microhardness was measured by the *Vickers* method (*ASTM E92*) at a load of 0.98 N on a *Wolpert Group 402MVD* hardness tester. Wear resistance under dry friction in reciprocating sliding was evaluated on a *Bruker UMT-2* tribometer using a ball-on-flat scheme in accordance with *ASTM G133-05*. The tests were carried out at a load of 25 N, a frequency of 5 Hz, and a duration of 1,800 s, with a total sliding distance of 90 m. A *WC–Co* (6 wt.% *Co*) ball with a diameter of 6.35 mm was used as the counterbody. The morphology of the worn surfaces was studied using a *Bruker Contour GT-K1* optical profiler. The volume of the worn material was determined from the profilometry data.

Results and discussion

Phase analysis of the cladded layers after combined treatment

Fig. 2,*a* shows the diffraction patterns of the substrate (*AISI 321* steel) and the coatings after combined treatment (quenching followed by hot rolling). The initial steel has a single-phase austenitic structure. The phase composition of the coatings after quenching and hot plastic deformation is a mixture of austenite (γ-*Fe*) and compounds of the Me_2B and $Me_{23}C_6$ types. The combined treatment leads to a shift in the positions of the austenite phase reflections relative to those of the substrate (Fig. 2,*b*). The largest shift is exhibited by the *C2QHR* coating with a higher boron content. Concurrently, an increase in the intensity of

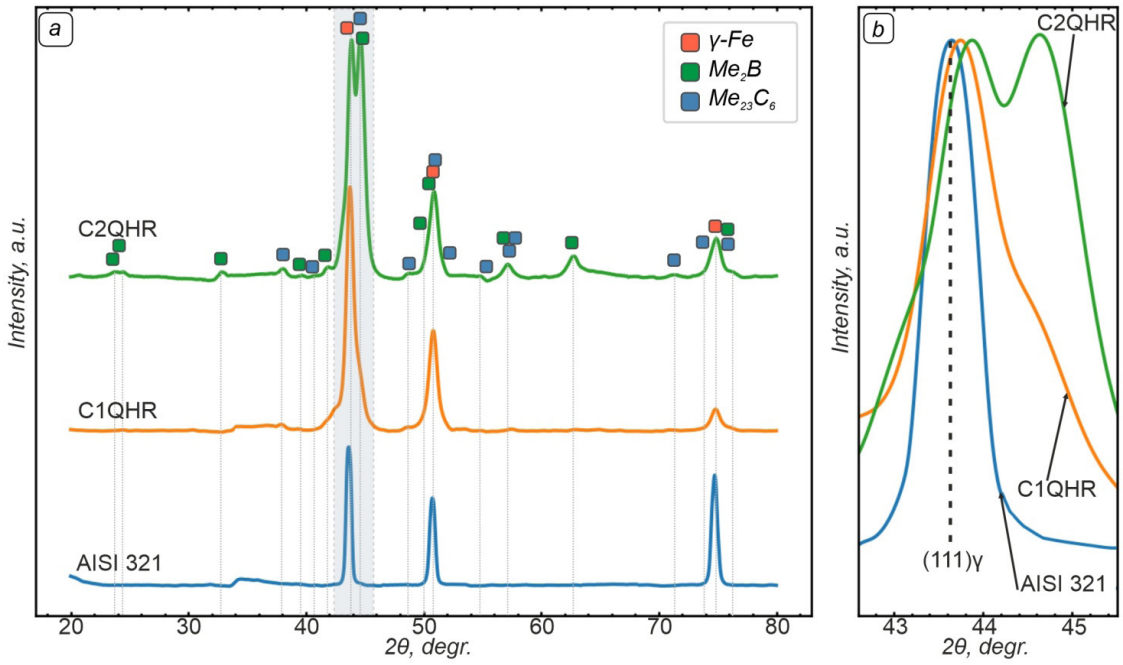

Fig. 2. Diffraction patterns obtained from the base material (*AISI 321*) and the coatings, normalized to the maximum intensity (*a*); enlarged view of the region indicated by the gray rectangle in (*a*), showing the shift of the (111)γ reflection (*b*)

the adjacent (111) reflection (angular position ~44.8°) is recorded, corresponding to a superposition of the Me_2B and $Me_{23}C_6$ diffraction maxima.

Microstructure of the cladded layers after combined treatment

The structure of the *C1QHR* and *C2QHR* coatings consists of an austenitic matrix containing coarse and fine strengthening precipitates (Fig. 3). Following the morphological classification proposed in [26], the coarse precipitates may be divided into three types: rod-shaped (type I) – elongated crystals with a predominantly rectilinear shape; coral-shaped (type II) – branched crystals with a characteristic dendritic morphology; and complex-shaped precipitates (Fig. 3*c*, *d*). The *C2QHR* coating, which has a higher boron content and a greater eutectic volume fraction (33 ± 6.42%), is dominated by coarse rod-like precipitates (type I). In contrast, the *C1QHR* coating, with lower boron content and a smaller eutectic fraction (15 ± 1.04%), predominantly features coral-like precipitates (type II) after combined treatment (quenching followed by hot rolling). The coral-shaped type II crystals display a more intricate branched structure and are located in the interdendritic spaces. The absence of massive rod-shaped crystals, which are observed in *C2QHR*, from the microstructure of *C1QHR* is due to insufficient boron concentration for the formation of coarse boride and borocarbide phases.

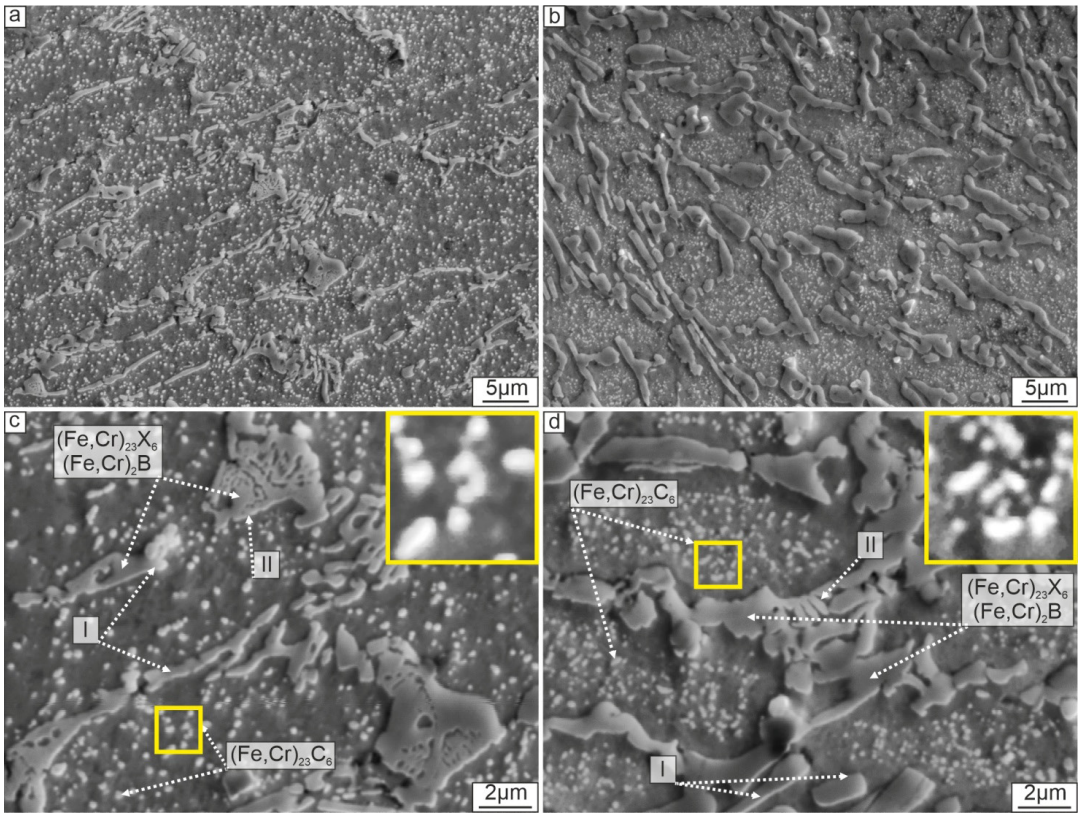

Fig. 3. Microstructure of the coatings: (*a*, *c*) *C*1*QHR*; (*b*, *d*) *C2QHR*

Elemental mapping of the cladded layers (exemplified by *C1QHR*, Fig. 4) revealed the following characteristic regions:

– regions enriched in iron and nickel, corresponding to the austenitic matrix;

– regions enriched in chromium, carbon, and boron, corresponding to the eutectic constituent;

– localized fine precipitates composed of titanium carbide and nitride.

The actual composition of the cladded layers was assessed by *EDX* analysis performed on cross-sections of the coatings. It should be noted that this method does not allow the quantitative determination of light elements, in particular boron, due to its low atomic number and the low energy of its characteristic X-ray radiation. However, the analysis of the distribution and content of heavy elements (*Fe*, *Cr*, *Ni*) revealed

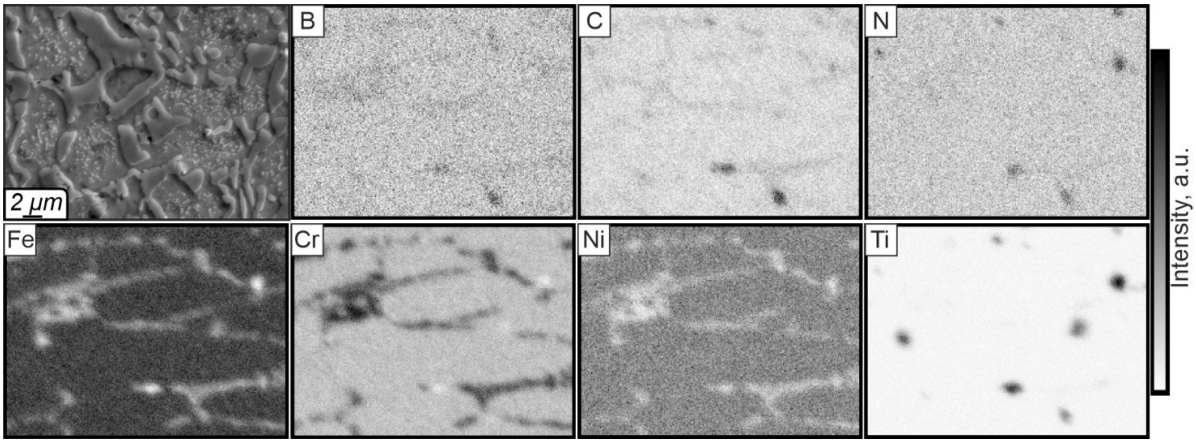

Fig. 4. Element distribution in the *C1QHR* coating

similar values for both compositions (Table 2), indicating significant dilution by the steel substrate. Hence, the formation of the *Fe–Cr–B* coatings results from the melting of the *AISI 321* steel and the intermixing of the molten substrate material with the alloying elements (chromium and boron) supplied from the powder mixture.

Table 2

Results of *EDS* analysis of the coatings in the cross-section

Coating	Elements (wt.%)		
	Fe	*Cr*	*Ni*
C1QHR	70.43 ± 2.69	20.02 ± 1.96	9.02 ± 1.15
C2QHR	70.19 ± 3.59	19.52 ± 3.30	9.71 ± 1.42

The formation of carbides, borides, and borocarbides in *Fe–Cr–B–C* system alloys is controlled by the quantitative ratio of boron to carbon [9, 27]. Although *EDX* analysis cannot provide quantitative determination of light elements, it permits qualitative evaluation of their distribution via the *B*/*C* intensity ratio.

The analysis of the elemental distribution in the *C1QHR* coating (Fig. 5,*a*) indicates that boron is concentrated in the eutectic constituents, while high-temperature exposure leads to the depletion of the matrix in chromium (a decrease in the *Cr*/*Fe* signal) and initiates the precipitation of fine $(Fe,Cr)_{23}C_6$ carbides within the austenite matrix. The precipitation of carbides is indirectly confirmed by the shift of the austenite diffraction peak (Fig. 2,*b*).

In the *C2QHR* coating (Fig. 5,*b*), hot deformation facilitates the formation of additional diffusion pathways for the alloying elements, resulting in enhanced local *B*/*C* ratio maxima in the eutectic regions and more severe chromium depletion of the austenitic matrix. These microstructural changes are reflected in the diffraction patterns by the increased intensity of peaks associated with boride phases (Fig. 2,*b*). Local maxima of the *Fe*/*Cr* ratio are observed, accompanied by phase coarsening. Concurrently with chromium depletion, fine carbide precipitates are formed, the volume fraction of which in the *C2QHR* coating is higher than in *C1QHR*, which is due to more intensive redistribution of alloying elements. It should be emphasized that boron, characterized by low diffusion mobility in austenite [1, 28], redistributes less than chromium and carbon, which explains its partial retention in the matrix even after high-temperature treatment.

Hardness of the cladded layers

Microhardness measurements were carried out on cross-sectional specimens along the direction from the cladded layer to the substrate. The average hardness of the *C1QHR* and *C2QHR* coatings after combined treatment was 429 ± 8 $HV_{0.1}$ and 484 ± 20 $HV_{0.1}$, respectively, which is 2.1–2.4 times higher than that of

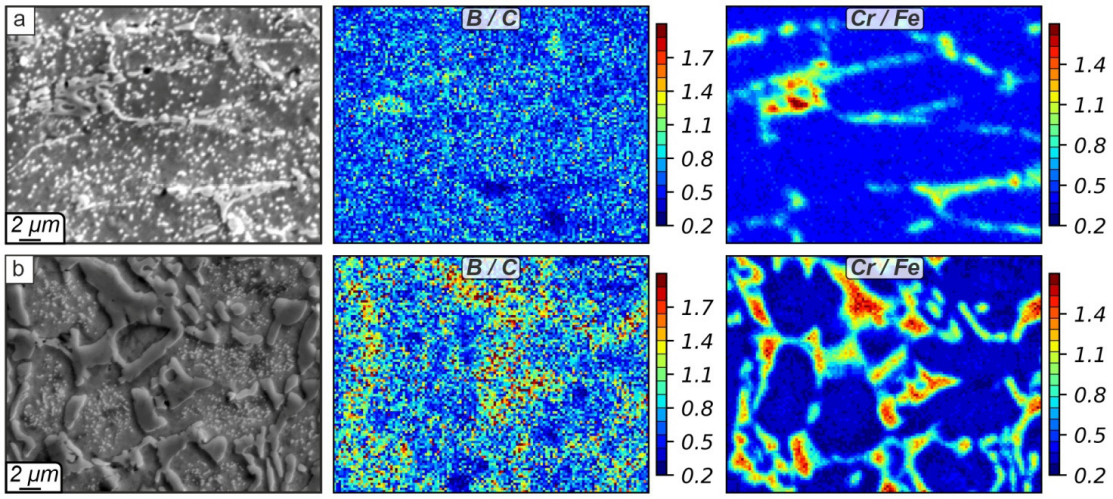

Fig. 5. B/C and *Cr/Fe* signal ratios obtained by *EDS* analysis for the (*a*) *C1QHR* and (*b*) *C2QHR* coatings

the *AISI 321* steel (~200 $HV_{0.1}$). This strengthening results from microstructure refinement, solid-solution hardening, and precipitation hardening caused by submicron $(Fe,Cr)_{23}C_6$carbide particles (Fig. 3).

Wear resistance tests

The analysis of the worn surface profiles (Fig. 6,*a*) showed that the friction process is accompanied by plastic deformation of the material and its displacement from the contact zone to the edges of the wear scar. The volume of the worn material was calculated using two methods: total volume – including the pile-up at the edges of the wear track, and lost volume – excluding the pile-up (the volume of the removed material). The largest amount of displaced material was observed for *AISI 321*, with an average wear track depth of about 78 μm and a wear volume of 356 × 10^6 $μm^3$. The wear track depth of the *C1QHR* and *C2QHR* coatings is about 38 μm and 24 μm, respectively, which corresponds to a 2-fold and 3.25-fold reduction relative

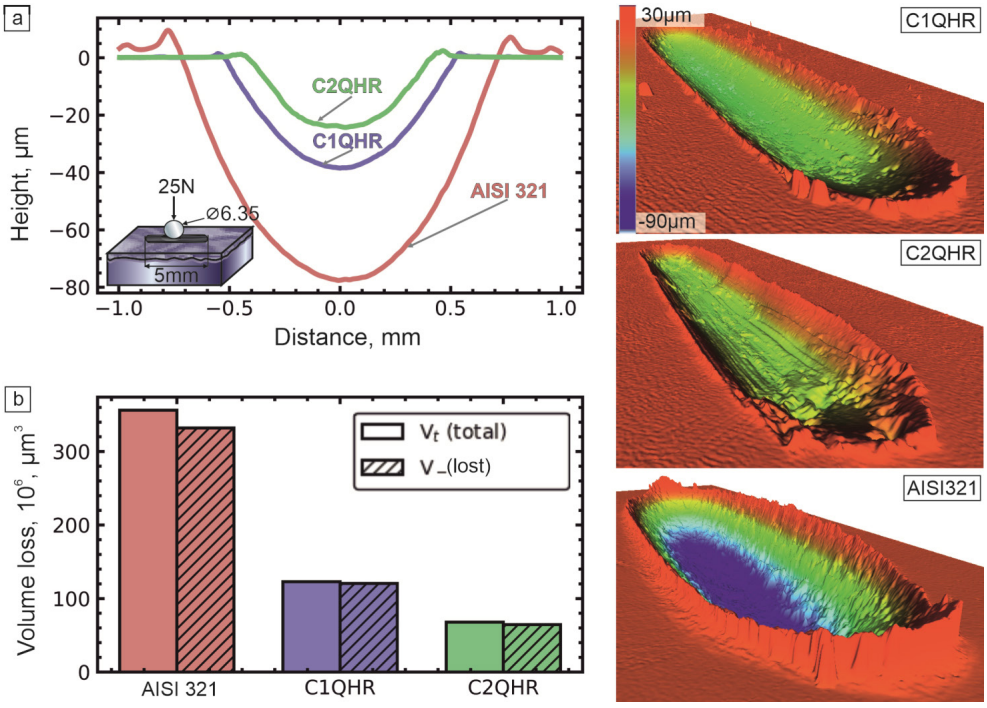

Fig. 6. Average profiles of wear tracks (*a*) and volume of worn material for the tested coatings and base material (*b*)

to the austenitic stainless steel. The wear volume was reduced by a factor of 2.9 for *C1QHR* and by a factor of 5.3 for *C2QHR* compared with the substrate material.

It should be noted that the *C1QHR* and *C2QHR* samples after quenching and hot rolling had different true strain values: $\bar{\varepsilon}_{\Sigma}$ = 0.96 (*C1QHR*) and $\bar{\varepsilon}_{\Sigma}$ = 0.67 (*C2QHR*). This is due to the different fraction of hardening phases. A twofold increase in boron content increases the eutectic volume fraction from 15 ± 1.04% to 33 ± 6.42%, thereby reducing the ductility of the *C2QHR* coating and inducing premature cracking during rolling. Thus, lower strain is a result of higher *B* content. It should be noted that hot rolling at 950 °C was carried out above the recrystallization temperature of austenite, facilitating stress relaxation in the substrate [29, 30]. Consequently, the hardening of the coatings was achieved not through deformation hardening, but through the precipitation of secondary phases, namely: $(Fe,Cr)_{23}C_6$ carbides, borides, and carboborides (Fig. 2, Fig. 3). Furthermore, both coatings exhibit identical phase compositions, consisting of an austenitic matrix with Me_2B and $Me_{23}C_6$ precipitates (Fig. 2). The only differences were in the volume fraction and morphology of the eutectic phases, which are governed by the chemical composition rather than by the strain level. These findings suggest that the observed variations in microhardness and wear resistance are predominantly controlled by the coating composition, not by strain level.

Typical friction coefficient curves as a function of testing time are shown in Fig. 7. The initial stage of the tests for all samples is characterized by a running-in period, accompanied by a gradual transition to a steady-state friction mode. It should be noted that the running-in behavior of the coatings is fundamentally different from that of the substrate steel. While significant fluctuations of the friction coefficient are observed at the initial stage for *AISI 321*, the *C1QHR* and *C2QHR* coatings exhibit a smoother transition to the steady-state mode. This indicates a reduced tendency towards seizure and adhesive wear due to the presence of hardening phases, which prevent the development of plastic deformation of the surface layer and localize the zone of frictional interaction. For *AISI 321* steel, the duration of the running-in stage under the given loading conditions is ~900 s. For the modified *C1QHR* and *C2QHR* coatings, the duration of the running-in stage is reduced by factors of approximately 2.2 and 4.5 compared with the initial steel, respectively. The average values of the friction coefficient in the steady-state mode are 0.72 ± 0.02 (*AISI 321*), 0.68 ± 0.01 (*C1QHR*), and 0.64 ± 0.02 (*C2QHR*). Thus, alloying with boron and chromium followed by quenching and hot plastic deformation enables a reduction in the friction coefficient to 0.64, which is 11% lower compared with the initial material. Notably, the achieved reduction in the friction coefficient is not in direct correlation with the increase in hardness, but is due to a change in the mechanisms of frictional interaction. As a result, it is possible to achieve a combination of high wear resistance, provided by the high hardness of the material, and a reduced friction coefficient, achieved through a change in the mechanism of contact interaction.

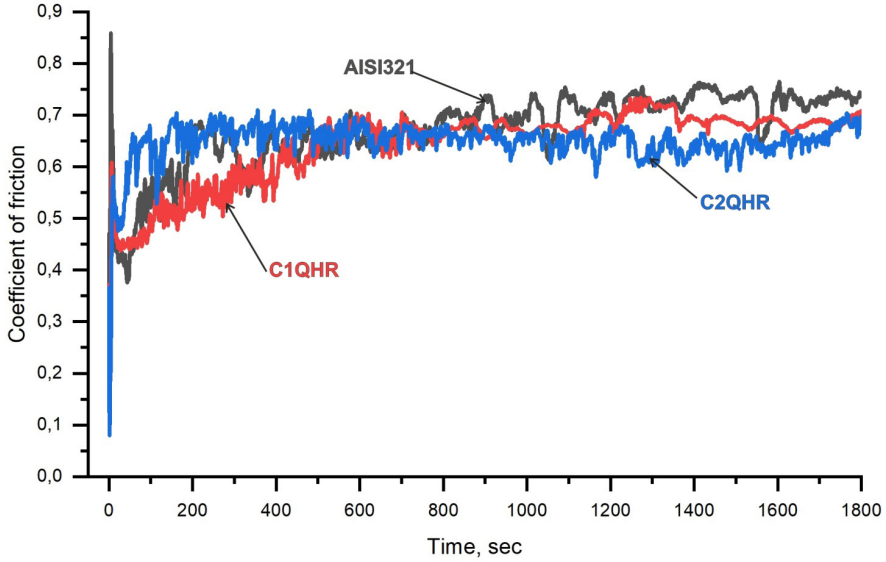

Fig. 7. Friction coefficient as a function of testing time

Fig. 8 shows images of the wear tracks and the results of *EDX* analysis of oxygen and tungsten on the worn surfaces of the *C1QHR* and *C2QHR* coatings. *EDX* analysis revealed the presence of tungsten on the worn surfaces of both coatings, which is a wear product of the *WC–Co* (*WC–6Co*) counterbody (Fig. 8, Table 3). In the *C1QHR* coating, the higher *W* content (up to 16.12 wt.%) correlates with the formation of extensive oxide films and the occurrence of an oxidative wear mechanism, whereas in *C2QHR*, with a lower *W* content (up to 4.26 wt.%), the abrasive component prevails, as evidenced by traces of micro-cutting on the friction surface. The decrease in chromium content in the austenitic matrix due to the precipitation of fine $(Fe,Cr)_{23}C_6$ carbides increases the ductility of the matrix, which facilitates the embedding of tungsten carbide particles into the surface layer of the coating. These particles, mixed with the wear debris of the coating itself, form a mechanically mixed layer ("third body") that protects the surface and reduces wear.

The friction surface of the *C1QHR* coating (Fig. 8,*a*, *c*, *d*) is characterized by the formation of extensive, predominantly continuous oxide films (Table 3), covering a significant portion of the wear track. These films have a heterogeneous morphology with local areas of delamination. The presence of pits indicates

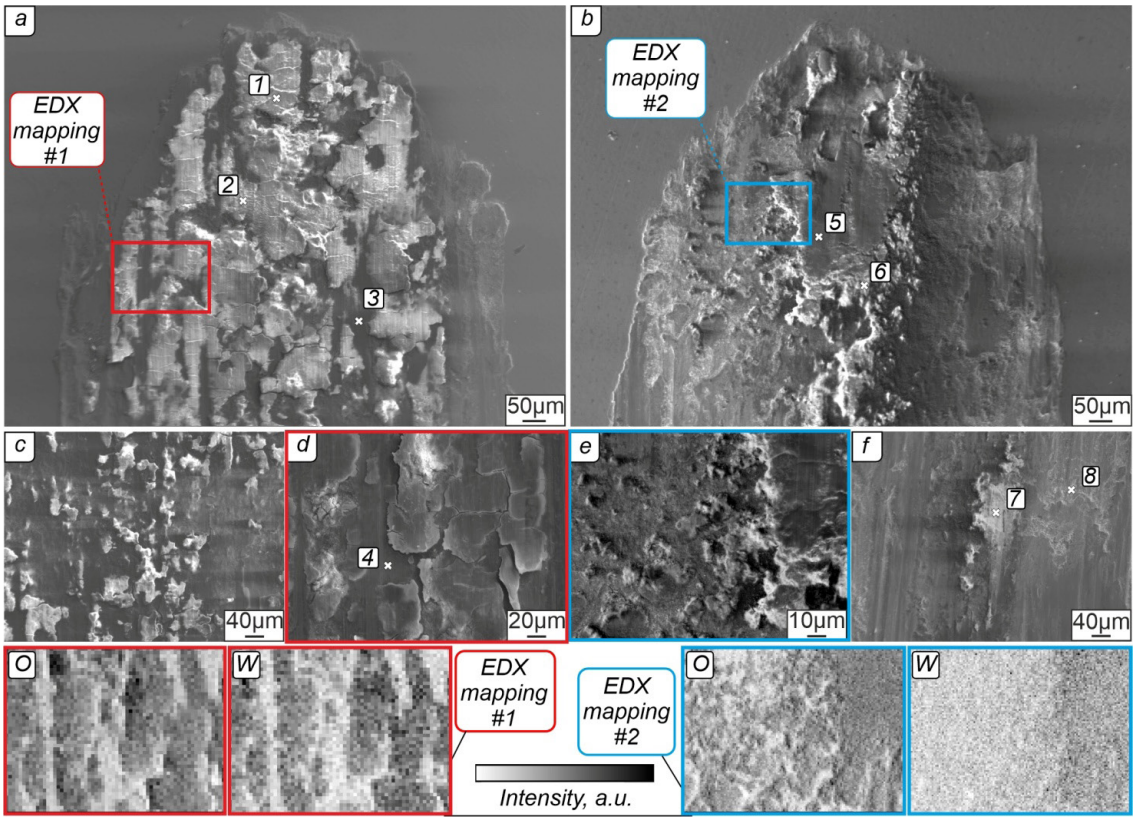

Fig. 8. Morphology of wear tracks for the (*a*, *c*, *d*) *C1QHR* and (*b*, *e*, *f*) *C2QHR* coatings; regions 1–8 indicate the locations of *EDS* point analysis, the results of which are presented in Table 2

Table 3

Element analysis of regions 1–8 in Fig. 8

Element (wt. %)	*C1QHR* coating				*C2QHR* coating			
	Point No.							
	1	2	3	4	5	6	7	8
Fe	33.99	33.79	37.96	54.19	40.70	46.09	40.79	12.94
Cr	9.89	9.91	11.30	23.12	11.52	13.43	11.82	61.05
Ni	4.34	4.19	4.75	6.06	5.75	6.41	5.72	9.33
W	16.12	15.64	12.43	3.63	3.93	2.76	4.26	–
O	35.41	36.26	33.29	12.77	37.78	30.98	37.03	16.23

that the oxide films, while performing a protective function, periodically break down under the action of cyclic contact loads through an oxidative-type wear mechanism. On the worn surface of *C2QHR* (Fig. 8,*b*, *e*, *f*), traces of micro-cutting in the form of parallel grooves oriented along the direction of counterbody movement prevail, which indicates the predominance of the abrasive component in the wear process.

Conclusions

1. *Fe–Cr–B*-based coatings were cladded onto *AISI 321* steel substrates by non-vacuum electron beam cladding. Iron was supplied to the coating from the substrate material, while chromium and boron were introduced from the powder mixture. A combined post-treatment, consisting of quenching from 1,100 °C followed by hot rolling at 950 °C, yielded true strain values of $\bar{\varepsilon}_{\Sigma} = 0.96$ for the *C*1*QHR* coating and $\bar{\varepsilon}_{\Sigma} = 0.67$ for the *C*2*QHR* coating.

2. The phase composition of the coatings consists of an austenitic matrix (**γ**-*Fe*) reinforced by Me_2B-type borides, $Me_2(C,B)$ carboborides, and $Me_{23}C_6$ carbides. A twofold increase in the boron content (*C1QHR* vs. *C2QHR* compositions) resulted in an increase in the volume fraction of the eutectic phases from 15 ± 1.04% to 33 ± 6.42%.

3. The maximum microhardness of the *C2QHR* coating was 484 ± 20 $HV_{0.1}$, which is 2.4 times higher than that of the *AISI 321* steel (~200 $HV_{0.1}$). The *C1QHR* coating exhibited a hardness of 429 ± 8 $HV_{0.1}$. The observed strengthening is attributed to precipitation hardening, structure refinement, and the presence of high-strength boride and carbide phases.

4. The *C2QHR* coating exhibited the highest wear resistance among the alloys studied under dry sliding conditions. The wear volume of the *C2QHR* coating was 5.3 times lower, and that of the *C1QHR* was 2.9 times lower, compared with the *AISI 321* substrate. The friction coefficient decreased from 0.72 (steel) to 0.64 (*C2QHR*). The improved wear resistance is provided by increased hardness and the formation of oxide films.

References

1. Hu C., Jiang Y., Quan J., Zong X., Lu Y., Li Y., Chen S. The retarding growth mechanism of boride layers on AISI 316L stainless steel: A combined experimental and DFT study. *Scripta Materialia*, 2025, vol. 269, p. 116899. DOI: 10.1016/j.scriptamat.2025.116899.

2. Xu J., Yang Y., Han H., Lei J., Di R., Fang Y. Enhancement of wear resistance and corrosion resistance of austenitic stainless steel by graphene nanoplatelets and titanium powders. *Ceramics International*, 2025, vol. 51 (23), pp. 38152–38165. DOI: 10.1016/j.ceramint.2025.06.051.

3. Zhao G., Zhang Y., Zhao H., Li J., Li H., Ma L. Study on the process optimization and wear resistance of electron beam cladding AlCoCrFeNi coating on 253MA austenitic stainless steel surface. *Materials Characterization*, 2023, vol. 205, p. 113341. DOI: 10.1016/j.matchar.2023.113341.

4. Veeramallu K., Krishna A.G. Enhanced wear and corrosion performance of stainless steel 316L with addition of different weight percentages of GNP. *Composites Theory and Practice*, 2024, vol. 24 (1), pp. 25–32. DOI: 10.62753/ctp.2024.04.1.1.

5. Wu T., Yang H., Xu G., Zhen Y., Han F., Zhang Y., Liu Y., Ji C., Wang K. Achieving ultrahigh wear resistance via laser remelting-induced nano-lamellar structures in FeCrB alloy coatings. *Surface and Coatings Technology*, 2025, vol. 517, p. 132840. DOI: 10.1016/j.surfcoat.2025.132840.

6. Chen C., Lv B., Ma H., Sun D., Zhang F. Wear behavior and the corresponding work hardening characteristics of Hadfield steel. *Tribology International*, 2018, vol. 121, pp. 389–399. DOI: 10.1016/j.triboint.2018.01.044.

7. Röttger A., Weber S., Theisen W. Supersolidus liquid-phase sintering of ultrahigh-boron high-carbon steels for wear-protection applications. *Materials Science and Engineering: A*, 2011, vol. 528 (13–14), pp. 4631–4638. DOI: 10.1016/j.msea.2011.10.118.

8. Shi X., Jiang Y. Analysis of morphological, thermodynamic, and mechanical properties of typical hard phase Fe–5Cr–1.5B–0.45C alloy. *Journal of Alloys and Compounds*, 2020, vol. 816, p. 152681. DOI: 10.1016/j.jallcom.2019.152681.

9. Lentz J., Röttger A., Theisen W. Mechanism of the Fe3(B,C) and Fe23(C,B)6 solid-state transformation in the hypoeutectic region of the Fe-C-B system. *Acta Materialia*, 2016, vol. 119, pp. 80–91. DOI: 10.1016/j.actamat.2016.08.009.

10. Röttger A., Lentz J., Theisen W. Boron-alloyed Fe–Cr–C–B tool steels – Thermodynamic calculations and experimental validation. *Materials & Design*, 2015, vol. 88, pp. 420–429. DOI: 10.1016/j.matdes.2015.08.157.

11. Berns H., Fischer A. Abrasive wear resistance and microstructure of Fe-Cr-C-B hard surfacing weld deposits. *Wear*, 1986, vol. 112 (2), pp. 163–180. DOI: 10.1016/0043-1648(86)90238-3.

12. Lentz J., Röttger A., Theisen W. Hardness and modulus of Fe2B, Fe3(C,B), and Fe23(C,B)6 borides and carboborides in the Fe-C-B system. *Materials Characterization*, 2018, vol. 135, pp. 192–202. DOI: 10.1016/j.matchar.2017.11.012.

13. Yi Y., Xing J., Lu Y., Fu H., Wan M., Yu L., Zheng Q., Ya C. Investigations on microstructure, mechanical properties and abrasion resistance of 4wt%Cr-2wt%Mn-2wt%Cu-Fe-B alloy. *Materials Characterization*, 2018, vol. 137, pp. 222–230. DOI: 10.1016/j.matchar.2018.01.038.

14. Acosta P., Lara A., Valenzuela R. Superplastic behavior of thermomechanically processed Fe-0.8B-1.3C-1.6Cr (wt%) alloy. *Materials Letters*, 1996, vol. 26 (1–2), pp. 97–101. DOI: 10.1016/0167-577X(95)00193-X.

15. Jiang Z.Q., Feng X.L., Shi J.F. Influence of heat treatment on structures and mechanical properties of cast Fe-B-C alloy. *Advanced Materials Research*, 2008, vol. 33–37, pp. 459–462. DOI: 10.4028/www.scientific.net/AMR.33-37.459.

16. Zhang H., Fu H., Jiang Y., Yu Z., Guo H., Lei Y., Zhou R., Cen Q. Effect of heat treatment on microstructure and property of Fe-Cr-B alloy. *Materialwissenschaft und Werkstofftechnik*, 2012, vol. 43 (11), pp. 931–941. DOI: 10.1002/mawe.201200939.

17. Cui G., Yang Z., Wang W., Gao G. Tribological properties of Fe(Cr)-B alloys at high temperature. *Journal of Central South University*, 2019, vol. 26 (10), pp. 2643–2650. DOI: 10.1007/s11771-019-4201-9.

18. Cui G., Wei J., Wu G. Wear behavior of Fe-Cr-B alloys under dry sliding condition. *Industrial Lubrication and Tribology*, 2015, vol. 67 (4), pp. 336–343. DOI: 10.1108/ILT-07-2014-0065.

19. Malyutina Yu.N., Pukhova E.A., Dudareva A.A., Batyrov B.B., Lazurenko D.V., Bataev I.A. Ni-Cr-Ti and Ni-Cr-Ti-B coatings prepared by nonvacuum electron beam cladding: Effect of boron and chromium on the microstructure, hardness and high-temperature oxidation resistance. *Materials Today Communications*, 2025, vol. 43, p. 111730. DOI: 10.1016/j.mtcomm.2025.111730.

20. Zimogliadova T.A., Bataev A.A., Lazurenko D.V., Bataev I.A., Bataev V.A., Golkovskii M.G., Saage H., Ogneva T.S., Ruktuev A.A. Structural characterization of layers fabricated by non-vacuum electron beam cladding of Ni-Cr-Si-B self-fluxing alloy with additions of niobium and boron. *Materials Today Communications*, 2022, vol. 33, p. 104363. DOI: 10.1016/j.mtcomm.2022.104363.

21. Ogneva T., Emurlaev K., Malyutina Y., Domarov E., Chakin I., Ruktuev A., Riabinkina P., Yurgin A., Bataev I. Heat treatment induced structural transformations and high-temperature oxidation behavior of $Al_{21}Co_{22}Cr_{22}Fe_{13}Ni_{22}$ high-entropy coatings produced by non-vacuum electron beam cladding. *Metals*, 2023, vol. 13 (10), p. 1689. DOI: 10.3390/met13101689.

22. Medvedeva N.I., Van Aken D.C., Medvedeva J.E. Stability of binary and ternary $M_{23}C_6$ carbides from first principles. *Computational Materials Science*, 2015, vol. 96, pp. 159–164. DOI: 10.1016/j.commatsci.2014.09.016.

23. Fu H., Xiao Q., Kuang J., Jiang Z., Xing J. Effect of rare earth and titanium additions on the microstructures and properties of low carbon Fe–B cast steel. *Materials Science and Engineering: A*, 2007, vol. 466 (1–2), pp. 160–165. DOI: 10.1016/j.msea.2007.02.032.

24. Macit C.K., Aksakal B., Horlu M. Enhancement on the tribological properties of 316L stainless steel via boron and alumina additions using mechanical alloying and powder metallurgy techniques. *Ceramics International*, 2025, vol. 51 (26), pp. 51549–51572. DOI: 10.1016/j.ceramint.2025.08.378.

25. Gao J., Ma J., Yang S., Guo Z., Ma J., Li H., Jiang Z., Han P. Grain boundary co-segregation of B and Ce hindering the precipitates of S31254 super austenitic stainless steel. *Journal of Materials Research and Technology*, 2023, vol. 24, pp. 2653–2667. DOI: 10.1016/j.jmrt.2023.03.135.

26. Berns H., Saltykova A., Röttger A., Heger D. Wear protection by Fe-B-C hard phases. *Steel Research International*, 2011, vol. 82 (7), pp. 786–794. DOI: 10.1002/srin.201000255.

27. Zhou Y., Chong X., Lin Y., Wang G., Jiang Y. Composition-dependent brittleness and ductility of the multicomponent phase $(Fe, Cr)_{23}(C, B)_6$ in Fe–Cr–B–C alloys: First-principles calculations and modeling. *Vacuum*, 2024, vol. 222, p. 113081. DOI: 10.1016/j.vacuum.2024.113081.

28. Li X., Wu P., Zhao S., Chen C., Yin R., Chen N. First-principle study of the solution type of boron in γ-iron. *Energy Procedia*, 2012, vol. 16, pp. 661–666. DOI: 10.1016/j.egypro.2012.01.107.

29. Zisman A.A., Soshina T.V., Khlusova E.I. Revealing prior austenite grains and analysis of the metadynamic recrystallization kinetics of austenite in hot rolled low carbon steel. *Letters on Materials*, 2012, vol. 2 (1), pp. 3–8. DOI: 10.22226/2410-3535-2012-1-3-8.

30. Razuvaev E.I., Kapitanenko D.V. Vliyanie termomekhanicheskoi obrabotki na strukturu i svoistva austenitnykh stalei [Effect of thermo-mechanical treatment on structure and properties of austenitic steels]. *Trudy VIAM = Proceedings of VIAM*, 2013, no. 5, p. 1–8.

Conflicts of Interest

The authors declare no conflict of interest.